Theory for Dual-Wavelength CO_2 Lidar Method to Distinguish Ice, Mixed-Phase, and Water Clouds

WYNN L. EBERHARD

Environmental Technology Laboratory, National Oceanic and Atmospheric Administration, Boulder, Colorado

(Manuscript received 23 July 1993, in final form 27 June 1994)

ABSTRACT

An analytical study shows that the ratio of backscatter from ice particles at two CO_2 lidar wavelengths is substantially different from the ratio from water drops. This forms the basis for a new method to discriminate between ice, water, and mixed-phase clouds. (The polarization technique often used by lidars operating in or near the visible part of the spectrum is not effective for CO_2 lidars, because depolarization from ice particles is usually very small at its infrared wavelength.) The effects of particle size distribution, differential attenuation in the cloud and clear air and other sources of uncertainty on the accuracy of the two-wavelength method are evaluated. Five wavelength pairs are examined to establish criteria for designing an optimum lidar.

1. Introduction

Determining whether a cloud is in water or ice phase is important for both radiative and microphysical studies. Cloud optical properties depend on the particle sizes, which are usually larger in ice clouds than in water clouds, on particle shape (usually quite nonspherical in ice clouds), and on phase-dependent refractive index at infrared wavelengths. Water or ice phase is important for understanding cloud formation and precipitation mechanisms, and mixed-phase information is helpful in studying glaciation and melting events. Shortwave lidars (defined in this context as those operating in or near the visible part of the spectrum where absorption within ice is small) can observe depolarization of backscatter to discriminate between ice or water phase in clouds (Sassen 1991). Wavelengths of 1064, 694, and 532 nm are commonly used. The laser transmits linearly polarized light, and the receiver detects the parallel and orthogonal components of the backscatter. The depolarization ratio (orthogonal/parallel) from water drops is small (<3%) because their spherical shape presents an azimuthal symmetry in the backscatter direction. For ice, the refraction and internal reflection of rays at nonnormal incidence on the crystal surfaces cause depolarization ratios of typically 50%. Sassen (1991) described the depolarization method and summarized applications performed by a large number of researchers.

A CO_2 lidar operates at a selected laser line between wavelengths of 9 and 11.5 μm in the infrared. Similar to shortwave lidars, CO_2 lidars have small depolarization ratios in backscatter from water drops. Unlike the case for shortwave lidars, however, ice particles absorb very strongly at CO_2 lidar wavelengths, so backscatter is dominated by reflection (with diffraction) from the surface facing the lidar. Analytical studies and experimental measurements by Eberhard (1992) showed that depolarization ratios in backscatter from ice clouds at 10.59-μm wavelength consequently remain small ($\sim$1%), although Gross et al. (1984) reported a brief experimental exception. A CO_2 lidar cannot apply the depolarization technique to discriminate between ice and water phase in clouds.

This study theoretically evaluates a different approach by which CO_2 lidars can detect cloud phase. The analysis shows that the ratio of backscatter at two appropriate wavelengths of a CO_2 lidar gives a clear signature for differentiating between water and ice particles. Several wavelength pairs, and the potential sources of error for each, are evaluated to guide wavelength selection for later implementation of the method.

2. Method

a. *Wavelength-dependent refractive index*

The volumetric backscatter cross section β of a collection of particles depends on their index of refraction n, their sizes relative to the wavelength, and their shapes. Figure 1 shows the real (n_r) and imaginary (n_i) parts of the index of refraction for water (Downing and Williams 1975) and ice (Warren 1984) as a function of wavelength λ over the range accessible by CO_2 lidar. The wavelength dependencies of ice and water are quite different between about 10.4 and 11.5 μm. This paper demonstrates that the ratio of backscatter,

Corresponding author address: Wynn Eberhard, NOAA/ERL, R/E/ET2, 325 Broadway, Boulder, CO 80303-3328.

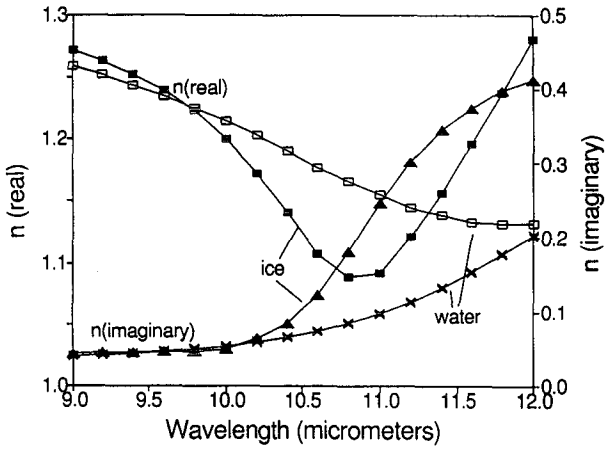

FIG. 1. Real and imaginary parts of the index of refraction for water and ice over the range of CO_2 laser wavelengths.

$$b(\lambda_1, \lambda_2) = \frac{\beta(\lambda_1)}{\beta(\lambda_2)}, \tag{1}$$

at two properly selected wavelengths, λ_1 and λ_2, depends primarily on the phase (water or ice) of the particles. Both wavelengths should satisfy $10.4 < \lambda < 11.5$ μm but should have only modest separation ($\lambda_1 - \lambda_2 \geq 0.5$ μm), so the changes in refractive index dominate the changes in scattering size parameter in determining b. Thus, b is only weakly dependent on particle sizes and shapes. This strong dependence of refractive index on wavelength and particle phase is the basis of the dual-wavelength method for ice–water discrimination.

Seven CO_2 lidar wavelengths (Table 1) were selected for this evaluation. The wavelengths are laser lines from both the common isotope $^{12}C^{16}O_2$ and the rare isotope $^{13}C^{16}O_2$ and are distributed over the 10.4–11.5-μm range. The wavelengths have been screened to avoid absorption by water vapor and ozone lines. Absorption by the water vapor continuum and CO_2 lines is still a complication and is discussed in section 3e. The high-gain lines, which are at the center of an absorption band, are technically attractive because they yield best pulse energy for a given pump power and laser cavity. The other lines were selected rather arbitrarily at wavelengths far from band center to illustrate the sensitivity of the technique to both wavelength and wavelength separation. The wavelength pair chosen for implementation must balance technical advantages like high pulse energy and low atmospheric absorption against the magnitude of the ice–water ratio. From the seven wavelengths, five pairs (Table 2) were formed for comparison to illustrate the factors important in the selection of an optimum set.

b. *Backscatter from water drops*

Scattering calculations can be used to predict the performance of the method and to develop algorithms for data analysis. Mie scattering (e.g., Bohren and Huffman 1983) can be applied with high accuracy to cloud drops, which are almost perfect spheres. We assumed drop size distributions $N(r)$ that are modified gamma in form. Using the notation of Hansen (1971), we have

$$N(r) = cr^{(1-3\nu)/\nu} \exp\left(-\frac{r}{r_e\nu}\right), \tag{2}$$

where r is drop radius, r_e is effective radius given by

$$r_e = \frac{\int r^3 N(r)\,dr}{\int r^2 N(r)\,dr}, \tag{3}$$

ν is a dimensionless variance of the size distribution, and c is proportional to number density (which cancels out in the ratio b). The mean radius is given by

$$r_m = \frac{\int rN(r)\,dr}{\int N(r)\,dr}. \tag{4}$$

The ratio of backscatter cross sections,

$$b_w(\lambda_1, \lambda_2) = \frac{\beta_w(\lambda_1)}{\beta_w(\lambda_2)}, \tag{5}$$

for two wavelength pairs are shown in Figs. 2 and 3 for a number of drop size distributions typical of those

TABLE 1. Potential CO_2 laser wavelengths and optics parameters for ice–water discrimination.

Wavelength (μm)	Isotope	Transition	Laser gain	Water		Ice		e^{-1} penetration depth (μm) in ice	$R_n(0°)$
				n_r	n_i	n_r	n_i		
10.441	$^{12}C^{16}O_2$	P(4)	low	1.187	0.0671	1.1334	0.0915	9.1	0.00574
10.591	$^{12}C^{16}O_2$	P(20)	high	1.179	0.0710	1.1089	0.1215	6.9	0.00597
10.639	$^{13}C^{16}O_2$	R(38)	low	1.174	0.0765	1.1015	0.1347	6.3	0.00642
10.738	$^{13}C^{16}O_2$	R(24)	high	1.169	0.0820	1.0919	0.1639	5.2	0.00802
10.910	$^{12}C^{16}O_2$	P(48)	low	1.160	0.0923	1.0889	0.2167	4.0	0.01244
11.194	$^{13}C^{16}O_2$	P(24)	high	1.145	0.114	1.1205	0.2993	3.0	0.02270
11.359	$^{13}C^{16}O_2$	P(38)	low	1.139	0.130	1.1476	0.3407	2.7	0.02916

TABLE 2. Wavelength pairs investigated for ice–water discrimination.

Wavelength (μm)			Typical backscatter ratio		Ice-to-water ratio	Figures of merit				
Higher λ_1	Lower λ_2	Difference $\lambda_1 - \lambda_2$	Ice b_i'	Water b_w'	X	Drop size variation F_s	Water cloud extinction F_e	Water vapor error F_m	Isotope	Laser gain
11.194	10.738	0.456	2.83	0.883	3.20	5.25	2.74	67	rare	high
10.910	10.441	0.469	2.17	0.761	2.85	4.52	3.00	85	common	low
11.194	10.591	0.603	3.80	0.792	4.80	7.10	3.01	75	both	high
11.359	10.639	0.720	4.55	0.876	5.19	7.67	2.60	42	rare	low
11.359	10.441	0.918	5.08	0.755	6.73	8.95	2.71	41	both	low

appearing in nature. Results for the widest wavelength pair, requiring different isotopes for each wavelength, are shown in Fig. 2, and results for one of the wavelength pairs from only one isotope are in Fig. 3. The values of b_w are comparable for the two wavelength pairs, and each exhibits only modest dependence on size distribution (restricted to ±23% in Fig. 2 and ±10% in Fig. 3). Table 2 includes a typical value b_w', which is defined as the average of b_w over $2 \leq r_m \leq 15$ μm and over the three values of ν (Figs. 2 and 3).

c. *Backscatter from ice particles*

Although the nonspherical shapes of ice crystals make accurate calculation of the ice particle backscatter cross section β_i very difficult, good results for

$$b_i(\lambda_1, \lambda_2) = \frac{\beta_i(\lambda_1)}{\beta_i(\lambda_2)} \tag{6}$$

can be obtained using gross simplifications. Calculations for ice spheres will be presented first, followed by calculations for infinitely long cylinders. Finally, a case for similar results for highly nonspherical particles like bullet rosettes will be made.

The value of b_i for spheres using Mie scattering calculations is shown in Fig. 4 for one wavelength pair and in Fig. 5 for another pair. These are gamma size distributions like those for the water drops but have nondimensional widths and a wider range of mean radii appropriate for ice particles. Infinitely long cylinders are more representative of long columns. Also shown in Figs. 4 and 5 are the calculations, based on the computer program of Bohren and Huffman (1983), for light incident in a direction normal to the cylinder axis. The results are quite close to those obtained for ice spheres. Based on these results, one can hypothesize that b_i is nearly independent of size distribution unless the radii are smaller than about 10 μm.

As a preface to estimating the behavior of b_i for the large variety of nonspherical shapes of ice particles, it is important to understand the principal features of backscatter at these wavelengths and size parameters. Table 1 gives the penetration distance D in solid ice through which absorption reduces the radiance by a

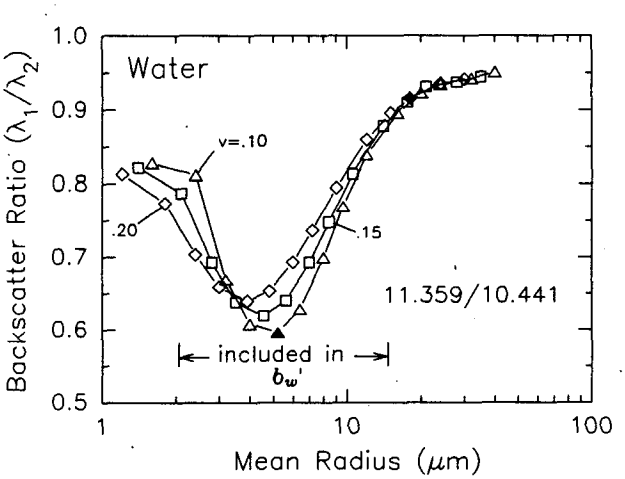

FIG. 2. Ratio b_w of backscatter cross section at wavelength 11.359 μm to that at 10.441 μm as a function of mean radius r_m and nondimensional width ν of the drop size distribution. The b_w' is the average of b_w for r_m between 2 and 15 μm. The filled symbols are values used to calculate the figure of merit F_s.

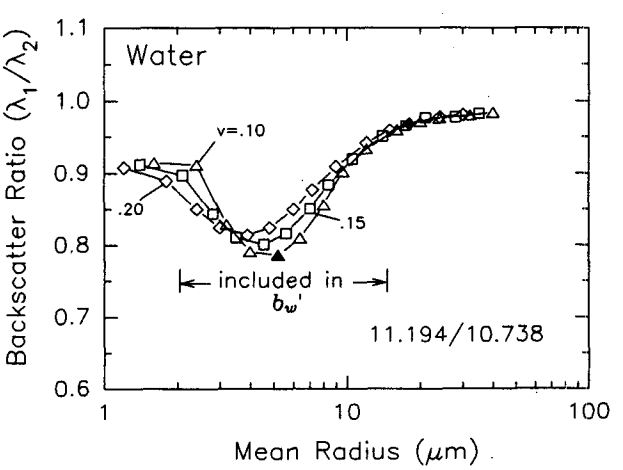

FIG. 3. Ratio b_w as in Fig. 2, but for 11.194- and 10.738-μm wavelengths.

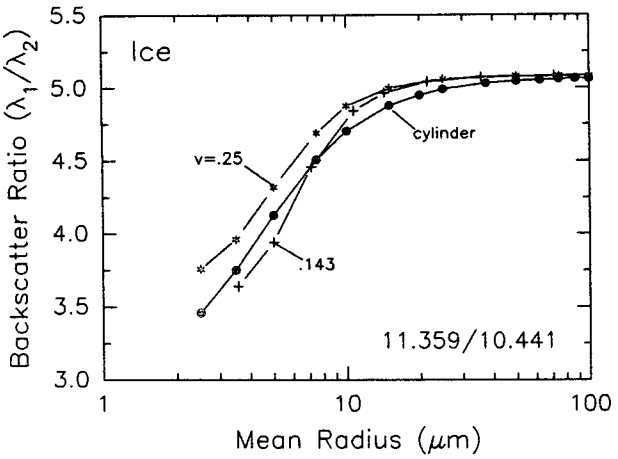

FIG. 4. Ratio b_i of backscatter cross section at wavelength 11.359 μm to that at 10.441 μm for distributions of ice spheres (crosses and asterisks) and for a distribution of infinitely long cylinders (filled circles) with light incident normal to the axis.

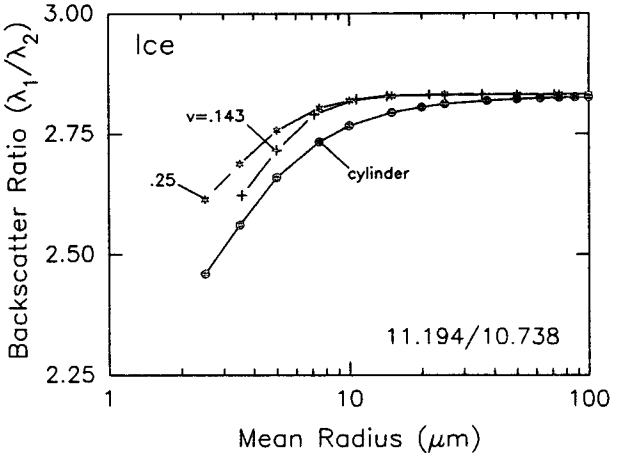

FIG. 5. Ratio b_i as in Fig. 4 but for 11.194- and 10.738-μm wavelengths.

factor of e. For large particles, the thickness t parallel to the lidar beam satisfies $t \gg D$ for these particles. As discussed by Bohren and Huffman (1983), the backscatter is then dominated by mirrorlike reflection from whichever part of the first surface is perpendicular to the beam. Bohren and Huffman use this simple model to calculate the backscatter cross section for a large absorbing sphere in the geometric optics limit ($r \gg \lambda$). We have confirmed that this result is identical to that obtained using Mie scattering. We have similarly confirmed the validity of this approach for a cylinder with large radius.

In the geometric optics limit for spheres and infinite cylinders, b_i is given by the wavelength ratio of $R_n(0°)$, which is the reflectivity for light normally incident on a thick slab. Here $R_n(0°)$, which is calculated from the Fresnel equations (e.g., Hecht and Zajac 1974), is listed in Table 1 for each wavelength. The resulting values of b_i, which are denoted as b_i' and listed in Table 2, agree very closely with the asymptotic values in Figs. 4 and 5. Indeed, particles of any shape with segments large enough to satisfy the geometric optics criterion are expected to have the same b_i' as large-radius spheres or cylinders.

Another important feature is the rapidity with which backscatter converges to the geometric optics value at these wavelengths as the size of the ice particle increases above approximately 10 μm. For both the spherical and infinite cylinder calculations, the familiar oscillatory behavior in β_i appears as the size parameter exceeds the Rayleigh limit, but the oscillations quickly damp out with increasing radius because of the strong absorption. The peaks and valleys do shift position as the wavelength changes from λ_1 to λ_2, but those with a significant swing in β_i shift by only a slight amount. Most ice particle size distributions are wide enough (Dowling and Radke 1990) to smooth out much of this oscillatory behavior. These factors, combined with the quick convergence of λ_i to the geometric optics value, are expected to keep b_i very close to b_i' for all kinds of particle shapes with segments that have dimensions no smaller than about 20 μm. Figures 4 and 5 suggest that deviations of b_i from b_i' will be modest even for segments or particles as small as 10 μm. Since particles this small are infrequent (Dowling and Radke 1990), the geometrical optics value b_i' is valid for most ice clouds that appear in nature.

d. Ice–water ratio

The computed values of b_w and b_i for all five wavelength pairs are summarized in Fig. 6. The b_w curves

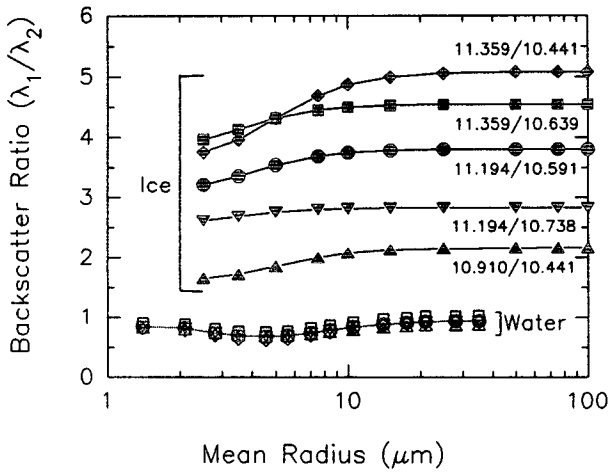

FIG. 6. Ratio of backscatter cross sections for the wavelength pairs indicated (μm) as a function of mean radius assuming spheres. Filled symbols are b_i for ice with $\nu = 0.25$; open symbols are b_w for water with $\nu = 0.15$; and the symbol outline is identical for water and ice for each wavelength pair.

all have similar magnitudes ($\approx$0.8) and shapes (dip minimum at $r_m \approx 5$ μm). The b_i curves are considerably different in magnitude for the five wavelength pairs (generally increasing with λ_1 and with $\lambda_1 - \lambda_2$) but have similar shapes (declining slightly with r_m less than 10 μm). The magnitude of the ice–water signature (Table 2) can be defined as

$$X(\lambda_1, \lambda_2) = \frac{b_i'(\lambda_1, \lambda_2)}{b_w'(\lambda_1, \lambda_2)}. \quad (7)$$

The larger value of b_i' compared with b_w and the weak dependence on particle sizes are the basis for this new method to discriminate ice and water clouds.

A lidar applying this concept must be able to measure backscatter at each wavelength in a pair. Measured values close to b_w' (or b_i') would reveal particles entirely or predominantly in water (or ice) phase.

e. *Mixed-phase ice fraction*

For mixed-phase clouds, one can define a linear equation in the measured b between the extreme cases of pure water or pure ice cloud according to

$$b = f b_i' + (1 - f) b_w'. \quad (8)$$

By substituting Eqs. (5) and (6) into Eq. (8), it can be shown that f is the fraction of the cloud composed of ice particles as weighted according to the backscatter cross section at λ_2; that is,

$$f = \frac{\beta_i(\lambda_2)}{\beta_w(\lambda_2) + \beta_i(\lambda_2)}. \quad (9)$$

Although f weighted by number density or by mass might be preferred in some applications, the weighting by $\beta(\lambda_2)$ should prove useful. The approximate value of ice fraction in the cloud can be found from the measured value b according to

$$f = \frac{b - b_w'}{b_i' - b_w'}. \quad (10)$$

3. Limitations to accuracy

Several sources of error exist that can limit the accuracy of the two-wavelength method, especially in determining f. This section discusses the relative importance of the principal sources of error.

a. *Drop size*

The theoretical ratio $b_w(\lambda_1, \lambda_2)$ exhibits some dependence on the r_m of the drop size distribution and, to a lesser extent, on the width ν of the size distribution (Figs. 2, 3, and 6). Figures 2 and 3 indicate that the greater the separation in wavelength, the larger the changes in b_w with size distribution parameters. The precise value of b_w to use in a lidar algorithm is uncertain unless the shape of the size distribution is known.

A figure of merit for drop size variations, F_s, that relates X to this drop size uncertainty is helpful for evaluating errors and optimizing wavelengths. The uncertainty in b_w for each wavelength pair can be represented by δ_w, defined as half the peak-to-valley ratio in the dip seen in Figs. 2 or 3. Using the filled diamond and triangle (Figs. 2 and 3) as the peak and valley values, respectively, we have

$$\delta_w = \frac{1}{2} \frac{b_w(r_m = 17.5\ \mu\text{m}, \nu = 0.20)}{b_w(\text{minimum for } \nu = 0.10)}. \quad (11)$$

The figure of merit is defined as

$$F_s(\lambda_1, \lambda_2) = \frac{X}{\delta_w}, \quad (12)$$

where larger values of F_s mean higher accuracy for interpreting the measured lidar ratio b. The list of values of F_s in Table 2 shows that accuracy improves as λ_1 and $\lambda_1 - \lambda_2$ increase over the range of wavelengths considered.

b. *Ice particle size*

The calculated results in Figs. 4–6 for ice spheres and cylinders reveal a growing departure from the geometric optics limit as particle mean radius r_m decreases below about 10 μm. A figure of merit was not defined for this uncertainty, because backscatter from actual small ice crystals with more complicated shapes might behave somewhat differently from that for the spherical and cylindrical shapes assumed here. Fortunately, ice particles this small are believed to be uncommon in clouds (Dowling and Radke 1990). This uncertainty is expected to be less of a problem than the uncertainty caused by unknown drop sizes.

c. *Water cloud extinction*

As the lidar probes deeper into a cloud, the intervening cloud increasingly attenuates the received energy. If the attenuation is the same for both wavelengths, the two-wavelength ratio method will be independent of optical depth. Figures 7–9 show, however, that attenuation cross sections are not the same for separate wavelengths in most water clouds. The results for water drops in Figs. 7 and 8 show stronger dependence on r_m than on ν.

The effect of wavelength-dependent extinction in a water cloud on the measured b is illustrated in Figs. 10 and 11. These calculations assume a cloud homogeneous in drop size distribution, except using τ_1 (one-way optical depth at λ_1) as a parameter allows the number density to vary. For size distributions with r_m smaller than about 4 μm, the extinction at the longer wavelength is stronger, and the extinction-reduced backscatter ratio measured by the lidar grows smaller

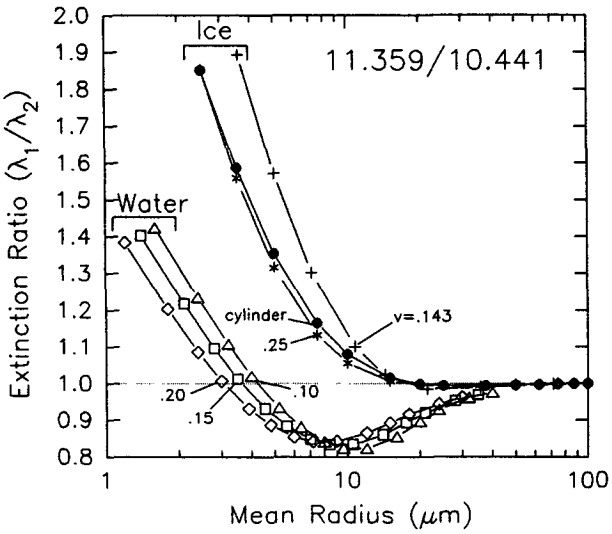

FIG. 7. Ratio of extinction cross sections at wavelengths of 11.359 and 10.441 μm for water drop size distributions as in Fig. 2 and for ice particle size distributions as in Fig. 4.

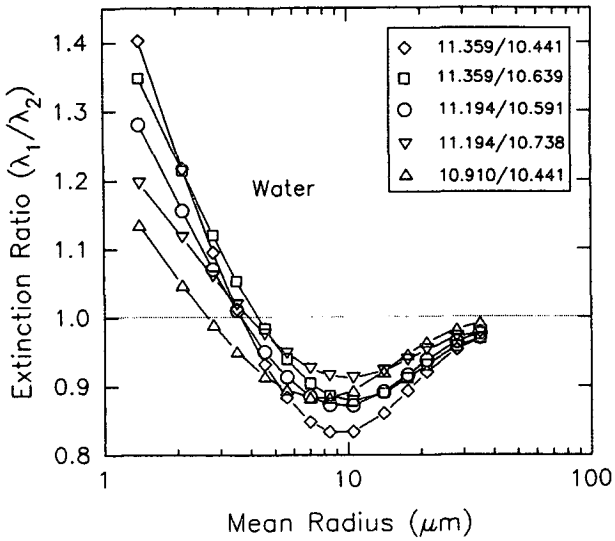

FIG. 9. Ratio of extinction cross sections for five wavelength pairs as a function of r_m for water drops with $\nu = 0.15$.

as optical depth increases. The opposite occurs for r_m larger than about 4 μm, and b grows larger with optical depth. The differential extinction is most pronounced for $r_m \approx 10$ μm and for $r_m < 2$ μm. The effect of differential extinction becomes more complicated when the size distribution (especially r_m) changes along the beam; this will be a common occurrence. Unless information is available about the drop size distribution, the differential extinction will make estimates of f difficult deep within the interior of mixed-phase clouds. Differential extinction in a thin water cloud may also make determination of the phase of a higher layer difficult. The range-average value of r_m obtainable through an extinction-to-backscatter algorithm like those proposed by Eberhard (1993a) and Platt and Takashima (1987) should prove helpful in removing some of the uncertainty in differential extinction in water clouds. Additional research is planned to include additional wavelengths to obtain a profile of r_m along the beam.

A reasonable measure of the uncertainty caused by differential extinction in water clouds can be assigned

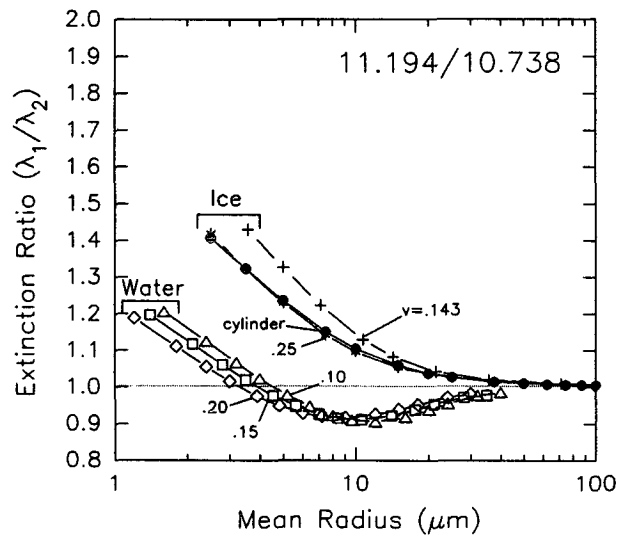

FIG. 8. Ratio of extinction cross sections as in Fig. 7 except for wavelengths of 11.194 and 10.738 μm.

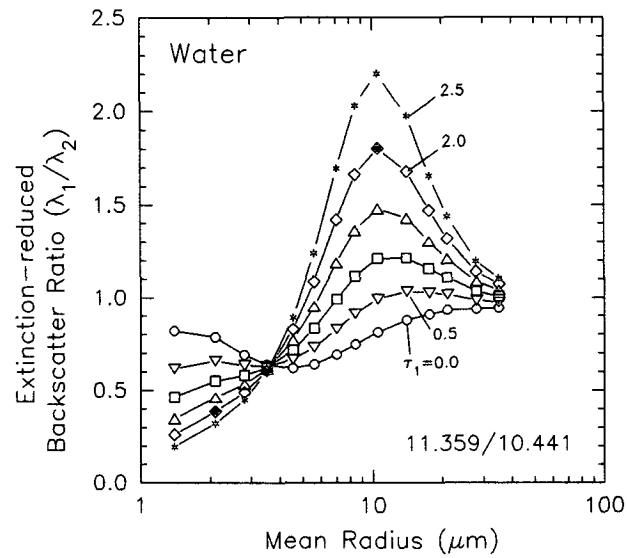

FIG. 10. Extinction-reduced backscatter ratio b_w ($\lambda_1 = 11.359$, $\lambda_2 = 10.441$ μm) in a water cloud with homogeneous size distribution (r_m as shown and $\nu = 0.15$) as a function of one-way optical depth τ_1 at λ_1. Filled symbols show values used to calculate the figure of merit, F_e.

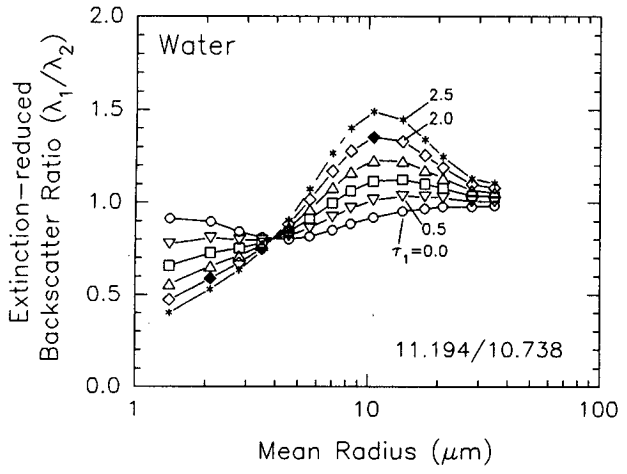

FIG. 11. Extinction-reduced b_w as in Fig. 10 except for $\lambda_1 = 11.194$ μm and $\lambda_2 = 10.738$ μm.

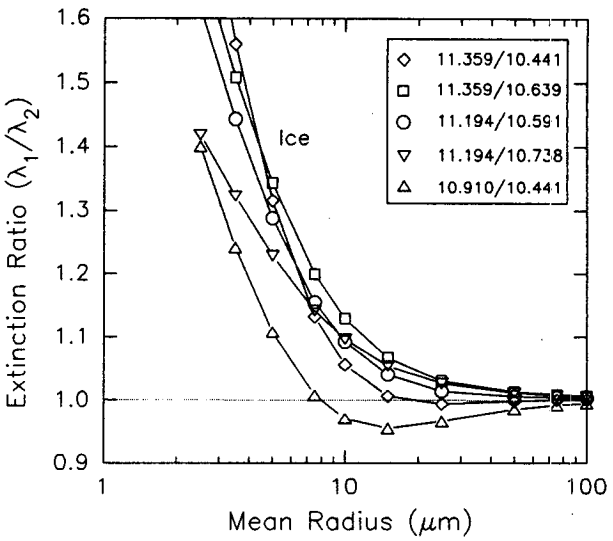

FIG. 12. Ratio of extinction cross sections for five wavelength pairs as a function of r_m for ice spheres with $\nu = 0.25$.

by assuming a one-way optical depth of $\tau_1 = 2$, where the round-trip transmission of the signal at λ_1 is only $e^{-4} = 1.8\%$. The range of observed signals can be represented well by the filled symbols in Figs. 3, 10, and 11, where $\nu = 0.15$ was assumed for the width of the size distribution. Half this range is given by

$$\delta_e = \frac{1}{2}\frac{b_w(r_m = 10.5\ \mu\text{m}, \tau_1 = 2)}{b_w(r_m = 2.1\ \mu\text{m}, \tau_1 = 2)}. \quad (13)$$

The figure of merit for water cloud extinction is defined as

$$F_e(\lambda_1, \lambda_2) = \frac{X}{\delta_e}. \quad (14)$$

The F_e values listed in Table 2 show little dependence on the choice of wavelength pair.

d. Ice cloud extinction

Calculations of extinction for ice spheres and cylinders in Figs. 7, 8, and 12 give some guidance. They suggest that differential extinction is small for $r_m \gtrsim 25$ μm, which includes most cirrus. The dependence on particle mean size seems stronger than on size distribution width or particle shape (Figs. 7 and 8). For r_m decreasing below about 10 μm, differential absorption grows exponentially such that the extinction-reduced b declines as optical depth increases. Most ice clouds have small optical depths and large particles, so differential absorption in cirrus is expected to be much less a problem than in water clouds.

e. Molecular absorption

Absorption of CO_2 laser radiation by the water vapor continuum and CO_2 lines is wavelength dependent. Differential molecular absorption should be accounted for in determining b. The roundtrip attenuation as a function of height to the target cloud is shown in Fig. 13 for seven wavelengths (Table 1), assuming an average midlatitude summer season atmospheric profile (McClatchey et al. 1972) and a vertically pointing lidar. Absorption by the water vapor continuum, which increases with wavelength, dominates for wavelengths from the rare isotope ($^{13}C^{16}O_2$) and for 10.910 μm. Absorption by the same CO_2 line as the laser uses dominates the molecular attenuation at 10.591 μm and is

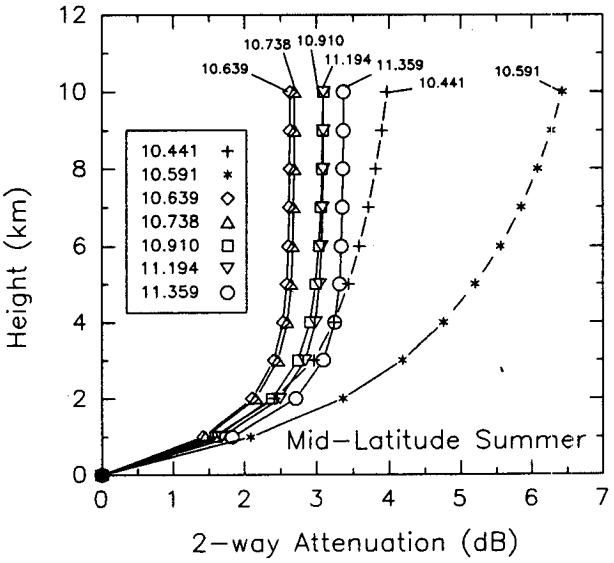

FIG. 13. Signal attenuation by water vapor and CO_2 for average midlatitude summer conditions as a function of height above a zenith-pointing lidar operating from the surface at the wavelengths listed in Table 1.

significant at 10.441 μm. Profiles of temperature, density, and water vapor (e.g., from radiosonde or seasonal models) permit correction of the measurements for molecular absorption.

A practical figure of merit for molecular absorption errors can be defined as X divided by the error in b for a mixed-phase cloud with $f = 0.5$, for which $b = 0.5(b_i' + b_w')$. The greatest uncertainty in calculating the differential absorption will arise from errors in the water vapor content. We assume a 25% undermeasurement ($\epsilon = -0.25$) of humidity over the path from the surface to a cloud at 7 km AGL. The figure of merit is

$$F_m = \frac{X}{0.5(b_i' + b_w')[(T_1^{-2}T_2^2)^{\epsilon} - 1]}, \quad (15)$$

where T_1 and T_2 are the correct one-way molecular transmissions between lidar and cloud at λ_1 and λ_2, respectively. The poorest values of F_m in Table 2 are for the two pairs with largest wavelength separation. All values of F_m are much larger than for F_s and F_e, however, so molecular absorption errors degrade the results much less than uncertainties in drop size and differential cloud extinction.

f. Calibration

The two-wavelength method uses the ratio of backscatter in two channels. A relative calibration is required between the two wavelength channels, which is much easier and more precise than an absolute calibration of the lidar. The differential effects of molecular absorption at the two wavelengths (section 3e) should be part of the calibration procedure. A target surface of a specific type and brand of sandpaper sheet tilted at 45° with respect to the lidar beam has proven practical for absolute calibration of pulsed CO_2 lidars (Post and Cupp 1990). The Jet Propulsion Laboratory of the National Aeronautics and Space Administration currently provides a service for measuring the reflectivity of targets with respect to sublimed flowers of sulfur, an accepted secondary standard, at requested CO_2 laser lines. An independent method like this should be applied to the calibration target for both lidar wavelengths used in ice–water discrimination. Once this reflectivity ratio of the target is known, calibrating the lidar on the target will determine any wavelength-dependent differences for the lidar as a unit, including telescope mirror reflectivity and detector sensitivity.

The shortwave depolarization method similarly requires only a relative calibration of the two polarization channels.

The accuracy of the two-wavelength method, especially for measuring the fraction of ice or water in mixed phase, depends directly on the accuracy of the relative calibration. Errors in the independent measurement of the ratio of target reflectivity and wavelength-different drifts in the lidar's sensitivity would lead directly to errors in the measured b.

g. Other

There are other sources of error that should be mentioned.

The value of the refractive index in Table 1 used for developing the algorithm could also be imperfect. From the discussion in Irvine and Pollack (1968) about laboratory measurement errors, one can conclude that n_r values for water and for ice are accurate to within 1.5% with a high degree of confidence. The values of n_i could easily be in error by as much as 10%, but an error exceeding 30% is quite unlikely. The *relative* error in n between a wavelength pair is probably much less than any absolute error, so uncertainties in n are not expected to cause much bias in the two-wavelength method.

Sometimes pristine ice crystals (plates or columns) orient themselves with the long axis horizontal and give rise to zenith-enhanced backscatter. The CO_2 lidar backscatter then shows diffraction effects that are zenith-angle dependent (Eberhard 1993b) and wavelength dependent. The width of the diffraction peak for backscatter from oriented plates scales as λ, and the peak backscatter for the lidar beam perpendicular to the face of the plate scales as λ^{-2}. In the worst case, zenith-enhanced backscatter could decrease b_i by as much as $(\lambda_1/\lambda_2)^{-2}$ when the lidar aims exactly at the vertical. The effect at several degrees off vertical in the tail of the diffraction peak is to increase b_i. The reduction in b_i at vertical for the largest wavelength separation in Table 2 is 18%, which is only a small fraction of X, so this is expected to be only a minor problem.

h. Expected accuracy

The CO_2 lidar two-wavelength backscatter ratio method has good capability for discriminating between ice and water clouds. The relative fraction of ice and water in mixed-phase clouds can also be measured. The complications discussed in this section, however, limit the accuracy in determining the ice fraction f. The complications can also mask the difference between a cloud parcel purely of one phase and a parcel containing a small fraction of particles in the other phase. The inverses of the figure of merit values in Table 2 give the approximate fractional accuracy expected for a measurement of f. If the data are corrected to first order for differential molecular absorption in clear air, the residual should cause little error. The values of F_s suggest a fundamental accuracy limitation in f, depending on wavelength pair, of 10%–20%, caused by the dependence on drop size distribution. An additional uncertainty can arise if ice particles are small (smallest dimension less than about 20 μm). As the lidar pulse penetrates to greater optical depth in a water

cloud, or in an ice cloud with small particles, the accuracy will decrease. At one-way optical depths of 2 in water clouds, the retrieved value of f should still be accurate within 30% or better.

4. Discussion

a. Optimum wavelength

The wider the wavelength separation and the larger the wavelengths within the range considered, the stronger the ice–water signature X. Most sources of error similarly tend to scale, however, with wavelength separation. Consequently, for these errors, section 3 and Table 2 show that the uncertainty in clearly defining cloud phase is about the same for all five wavelength pairs. An important exception is the sensitivity to changes in the drop size distribution; larger wavelength separation gives better accuracy. A wide separation is preferred, especially if the accuracy of cross-wavelength calibration does not diminish with increasing separation.

b. Lidar for initial tests

A conceptual diagram of the lidar under development for DIAL (differential absorption of light) applications, as well as a testing of the ice–water method, is shown in Fig. 14. The lasers and amplifiers are in a master-oscillator, power-amplifier configuration. The low-pressure CO_2 gas is excited by radio frequency (RF) in a microwave resonant cavity (Pearson 1993) rather than by electrical discharge of atmospheric-pressure gas as in our older system (Post and Cupp 1990). Operation of $^{13}C^{16}O_2$ low-pressure, electric discharge lasers has been demonstrated (e.g., Freed 1982). Our laboratory is currently investigating RF excitation of this isotope, which provides the wavelengths preferred for the ice–water method. The expense of this isotope is moderate, because these lasers and amplifiers require only a small amount. The final choice of wavelengths will depend on technical limitations of the lidar system in combination with the theoretical expectations found in this study.

The same isotope will initially be used in both continuous-wave (CW) laser oscillators and the laser amplifiers. (It may also be possible to fill each oscillator with a different isotope and the amplifiers with both isotopes for dual-isotope operation.) The oscillators will operate on different CO_2 lines. The shutters select which of the CW outputs is amplified and transmitted to the cloud and also to the detector as a local oscillator beam. When the acousto-optic modulator is pulsed, it forms a pulse from the incident CW beam and diverts it through the optical amplifiers, whose RF excitation is synchronously pulsed. Coherent mixing of the radiation backscattered from the atmosphere with the local oscillator provides quantum-limited sensitivity, overcoming the large thermal noise in the detector.

Another approach for two-wavelength generation involves only one local oscillator with wavelengths switched by angular adjustments of the diffraction grating that selects the operating laser line.

The lidar preferably would operate simultaneously at both wavelengths to avoid uncertainty arising from cloud density variations between pulses. Such a configuration would be unduly complicated for initial tests of the technique. Alternating wavelengths rapidly and averaging backscatter measurements over a few of these cycles to smooth variations should be satisfactory in most applications. The RF-excited lidar can switch rapidly and perform the alternating scheme well because it is expected to operate at high pulse rates (~500 Hz) and low pulse energies (~2 mJ), and it requires averaging of pulses anyway for adequate signal-to-noise ratio for detecting many clouds.

c. Plans for field validation

An initial field test of the two-wavelength method is planned when the new lidar is ready. Confirmation of the results can be obtained from some clouds based on temperature; clouds forming and residing in air warmer than 0°C will be completely water, and clouds colder than −40°C will be completely ice. Simultaneous shortwave lidar depolarization measurements or aircraft microphysics data on clouds of any temperature,

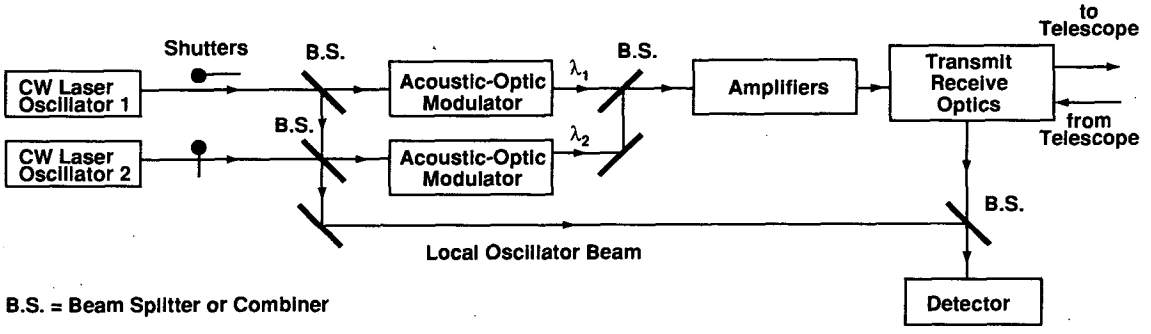

FIG. 14. Conceptual design of two-wavelength lidar system planned for testing the ice–water technique.

including mixed-phase clouds, will provide additional information for comparison. Elements of this test will include demonstration of two-wavelength lidar operation, evaluation of the stability of the relative calibration, and field confirmation of the predicted ratios b_i and b_w for pure-phase clouds and X. Demonstration of the utility of the method in measuring mixed-phase fraction f will also be sought.

d. *Comparison with shortwave depolarization method*

The CO_2 two-wavelength is expected to perform as successfully as the shortwave depolarization method (Sassen 1991) in many respects. Both techniques are ratio methods, which is a highly desirable feature for practical application. Each technique has advantages and disadvantages.

The CO_2 method has the advantage of theoretical simplicity. Simple algorithms for signal interpretation were developed in this study, whereas difficult empirical measurements, followed later by difficult scattering calculations on nonspherical particles, were required for the depolarization method. Field testing of the CO_2 method is needed, however, to validate the theory presented here.

Slight changes in the depolarization ratio for shortwave lidars can be used to determine crystal habit (Sassen 1991). Unfortunately, the CO_2 two-wavelength method cannot duplicate this capability.

The two-wavelength method has good potential for observing mixed-phase clouds if errors are kept small. The depolarization method has already demonstrated a similar capability (e.g., Sassen and Dodd 1988).

Multiple scatter is often a problem for shortwave lidars, particularly as the pulse penetrates into a dense water cloud. The depolarization grows as the degree of multiple scatter builds, giving ambiguous results. [Shortwave lidars with extremely narrow beam and field of view, e.g., approximately 0.3 mrad (Grund and Eloranta 1991) are an exception.] For coherent CO_2 lidar systems, multiple scatter is negligible, mainly because of the lidar's narrow field of view and the large angular width in the forward diffraction peak. The CO_2 method suffers errors from differential extinction in clouds, however, which can lead to uncertainties similar to those from multiple scatter in shortwave lidars.

When shortwave lidars experience zenith-enhanced backscatter from oriented ice crystals, the depolarization ratio can decline dramatically, and the measurement can be misleading. The CO_2 method is less hampered by zenith-enhanced backscatter, because it causes only small changes in the ice cloud signature.

One practical advantage of the CO_2 method is the inherent eye safety of the lidar, whereas precautions must be exercised when most shortwave lidars are operated. On the other hand, the CO_2 approach requires more complicated hardware, partly to achieve coherent detection and partly to generate two wavelengths. Although correction of the CO_2 lidar signal for molecular absorption is straightforward, it does place an additional burden on data processing.

5. Summary

The change with wavelength of the index of refraction of ice is quite different from that of water over the range 10.4–11.5 μm. Scattering calculations demonstrate that the ratio of backscatter from water clouds [Eq. (5)] at two adequately separated wavelengths is slightly less than unity, whereas the backscatter ratio from ice clouds [Eq. (6)] ranges from about 2 to 5 (Fig. 6), depending on the choice of wavelengths. The dependence on drop size distribution and on ice particle shapes and size distribution is much weaker. This analysis demonstrates the feasibility of discriminating between ice and water clouds by measuring the ratio of backscatter at two wavelengths using a pulsed CO_2 lidar. The approximate fractions of ice and water in mixed-phase clouds can also be measured, although accuracy decreases with probing depth into the cloud because of differential extinction. A wider wavelength separation provides a stronger ice–water signature, X, but some of the uncertainties tend also to scale with the wavelength separation.

The depolarization technique often used by shortwave lidars (Sassen 1991) fails for CO_2 lidar (Eberhard 1992), because depolarization from ice particles usually is very small ($\sim 1\%$). The strong absorption by ice particles at these infrared wavelengths keeps the depolarization small compared to the nonabsorbing case at shorter wavelengths. The CO_2 two-wavelength method is expected to perform well as an alternative to the shortwave depolarization method for discriminating whether a cloud is principally ice, water, or mixed-phase. The CO_2 method does require more complicated lidar hardware than the depolarization method. Except for shortwave lidars with extremely narrow beam and field of view, the depolarization method suffers inaccuracy from multiple scatter when the pulse penetrates deeply into a cloud, but the CO_2 method has a similar problem caused by differential extinction. The coherent CO_2 method enjoys the advantages of theoretical simplicity, complete eye safety, and less error in signal from oriented ice crystals.

Acknowledgments. The author thanks Kathleen Healy, John Bevilacqua, and Brent Gordon for contributions to software development, calculations, and figure preparation. Guy Pearson, Kin Pui Chan, and Barry Rye are the principals in developing the two-wavelength lidar. Michael Hardesty has provided valuable ideas and encouragement. Funding was provided through Grants DE-FG02-90ER61059 and DE-AI03-94ER61760 of the Department of Energy's Atmospheric Radiation Measurement Program and a grant

from the Climate and Global Change Program of the National Oceanic and Atmospheric Administration.

REFERENCES

Bohren, C. F., and D. R. Huffman, 1983: *Absorption and Scattering of Light by Small Particles.* John Wiley and Sons, 530 pp.

Dowling, D. R., and L. F. Radke, 1990: A summary of the physical properties of cirrus clouds. *J. Appl. Meteor.*, **29,** 970–978.

Downing, H. D., and D. Williams, 1975: Optical constants of water in the infrared. *J. Geophys. Res.*, **80,** 1656–1661.

Eberhard, W. L., 1992: Ice cloud depolarization of backscatter for CO_2 and other infrared lidars. *Appl. Opt.*, **31,** 6485–6490.

——, 1993a: CO_2 lidar technique for observing characteristic drop size in water clouds. *IEEE Trans. Geosci. Remote Sens.*, **31,** 56–63.

——, 1993b: Progress in interpreting CO_2 lidar signatures to obtain cirrus microphysical and optical properties. FIRE Cirrus Science Results 1993, NASA, 62–63.

Freed, C., 1982: Status of CO_2 isotope lasers and their applications in tunable laser spectroscopy. *IEEE J. Quantum Elec.*, **QE-18,** 1220–1228.

Gross, A., M. J. Post, and F. F. Hall, Jr., 1984: Depolarization, backscatter, and attenuation of CO_2 lidar by cirrus clouds. *Appl. Opt.*, **23,** 2518–2522.

Grund, C. J., and E. W. Eloranta, 1991: University of Wisconsin high spectral resolution lidar. *Opt. Eng.*, **30,** 6–12.

Hansen, J. E., 1971: Multiple scattering of polarized light in planetary atmospheres. Part II: Sunlight reflected by terrestrial water clouds. *J. Atmos. Sci.*, **28,** 1400–1426.

Hecht, E., and A. Zajac, 1974: *Optics.* Addison-Wesley, 565 pp.

Irvine, W. M., and J. B. Pollack, 1968: Infrared optical properties of water and ice spheres. *Icarus,* **8,** 324–360.

McClatchey, R. A., R. W. Fenn, J. E. A. Selby, F. E. Volz, and J. S. Garing, 1972: Optical properties of the atmosphere (revised). Air Force Cambridge Research Laboratories AFCRL-72-0497, 108 pp.

Pearson, G. N., 1993: A high pulse repetition frequency CO_2 Doppler lidar for atmospheric measurements. *Rev. Sci. Inst.*, **64,** 1155–1157.

Platt, C. M. R., and T. Takashima, 1987: Retrieval of water cloud properties from carbon dioxide laser soundings. *Appl. Opt.*, **26,** 1257–1263.

Post, M. J., and R. E. Cupp, 1990: Optimizing a pulsed Doppler lidar. *Appl. Opt.*, **29,** 4145–4158.

Sassen, K., 1991: The polarization lidar technique for cloud research: A review and current assessment. *Bull. Amer. Meteor. Soc.*, **72,** 1848–1866.

——, and G. C. Dodd, 1988: Homogeneous nucleation rate for highly supercooled cirrus cloud droplets. *J. Atmos. Sci.*, **45,** 1357–1369.

Warren, S. G., 1984: Optical constants of ice from ultraviolet to the microwave. *Appl. Opt.*, **23,** 1206–1223.